

1 **A new optical cell for *in situ* Raman spectroscopy, and its application to study**  
2 **sulfur-bearing fluids at elevated pressures and temperatures**

3

4 Marcel Dietrich<sup>1,2</sup>, Harald Behrens<sup>1,\*</sup>, Max Wilke<sup>3,2</sup>

5

6 <sup>1</sup> *Leibniz Universitaet Hannover, Institute of Mineralogy, Callinstrasse 3, 30167, Hannover, Germany*

7 <sup>2</sup> *Helmholtz-Centre Potsdam, Section 3.3, Chemistry and Physics of Earth Materials, Telegrafenberg,*  
8 *14473, Potsdam, Germany*

9 <sup>3</sup> *Universität Potsdam, Institute für Erd- und Umweltwissenschaften, Karl-Liebknecht-Str.24-25, 14476,*  
10 *Potsdam-Golm, Germany*

11 \* *Author for correspondence: [h.behrens@mineralogie.uni-hannover.de](mailto:h.behrens@mineralogie.uni-hannover.de)*

13

14

15 **Revision 2, submitted at November 14, 2017**

16

## ABSTRACT

17

18

19

20

21

22

23

24

Sulfur is an important component in volcanic gases at the Earth surface but also present in the deep Earth in hydrothermal or magmatic fluids. Little is known about the evolution of such fluids during ascent in the crust. A new optical cell was developed for *in situ* Raman spectroscopic investigations on fluids allowing abrupt or continuous changes of pressure up to 200 MPa at temperatures up to 750 °C. The concept is based on a flexible gold bellow, which separates the sample fluid from the pressure medium water. In order to avoid reactions between aggressive fluids and the pressure cell, steel components in contact with the fluid are shielded by gold foil.

25

26

27

28

29

30

31

32

33

34

35

36

37

38

The cell was tested to study redox reactions in fluids using aqueous ammonium sulfate solutions as a model system. During heating at constant pressure of 130 MPa, sulfate ions transform first to  $\text{HSO}_4^-$  ions and then to molecular units such as  $\text{H}_2\text{SO}_4$ . Variation of pressure shows that the stability of sulfate species relies on fluid density, i.e. highly charged species are stable only in high-density fluids. Partial decomposition of ammonium was evident above 550 °C by the occurrence of a nitrogen peak in the Raman spectra. Reduced sulfur species were observed above 700 °C by Raman signals near  $2590\text{ cm}^{-1}$  assigned to  $\text{HS}^-$  and  $\text{H}_2\text{S}$ . No clear evidence for the formation of sulfur dioxide was found in contrary to previous studies on aqueous  $\text{H}_2\text{SO}_4$ , suggesting very reducing conditions in our experiments. Fluid-mineral interaction was studied by inserting into the cell a small, semi-open capsule filled with a mixture of pyrite and pyrrhotite. Oxidation of the sample assembly was evident by transformation of pyrite to pyrrhotite. As a consequence, sulfide species were observed in the fluid already at temperatures of  $\sim 600\text{ °C}$ .

39 Keywords: *in situ* Raman spectroscopy, fluids, decompression, optical cell, sulfur speciation,  
40 redox reactions

41

## INTRODUCTION

42

43

44

45

46

47

48

49

50

51

Aqueous fluids, especially when containing sulfur, play an important role in the degassing of magmas and in the formation of hydrothermal ore deposits. Large quantities of sulfur are released to the atmosphere by active and passive degassing of magmas, having an important impact on global sulfur budget and hence, on the evolution of climate. Furthermore, the potential of hydrothermal fluids to transport ore-forming metals is affected by sulfur species, which may strongly increase the solubility of metals by formation of complexes (Pokrovski et al. 2008). Sulfur-bearing gases are also of technical interest, e.g., in fining of melts during industrial glass production the temperature-induced decomposition of sulfate in the melt (reaction:  $\text{SO}_4^{2-} = \text{SO}_2 + \frac{1}{2} \text{O}_2 + \text{O}^{2-}$ ) is used to enlarge bubbles and thus to increase their buoyant rise, enhancing the removal of bubbles (Müller-Simon 2011).

52

53

54

55

56

57

58

59

60

61

62

63

For modeling of melt degassing and formation of magmatic ore deposits, knowledge of the speciation of sulfur in gases and fluids in function of temperature, pressure, oxygen fugacity ( $f\text{O}_2$ ), sulfur fugacity ( $f\text{S}_2$ , often difficult to constrain) and fluid composition is needed (Burgisser et al. 2010, 2011). The Earth's surface and shallow crust are characterized by a large variation in sulfur speciation, with sulfide ( $\text{S}^{\text{II}-}$ ; as  $\text{H}_2\text{S}$ ,  $\text{HS}^-$  or  $\text{S}^{2-}$ ), sulfur dioxide ( $\text{S}^{\text{IV}+}$  as  $\text{SO}_2$ ) and sulfate ( $\text{S}^{\text{VI}+}$ ; as  $\text{H}_2\text{SO}_4$ ,  $\text{HSO}_4^-$  and  $\text{SO}_4^{2-}$ ) being the most common (e.g. Symonds et al. 1994; Self 2005; Self and Blake 2008; de Moor et al. 2013). Other sulfur species (for instance, elemental sulfur, sulfite, thiosulfate, polysulfides, polythionates, and organic sulfur) form as reaction intermediates in the sulfate-sulfide redox cycle but are relatively minor or thermodynamically metastable at near surface conditions (Pokrovski and Dubrovinsky 2011). The sulfur speciation in deep and hot fluids from hydrothermal magmatic systems and subduction zones hosting the major part of metallic resources on Earth is far less constrained, because such data are difficult to access

64 experimentally. Recent studies of Pokrovski and Dubessy (2015) indicate that intermediate-  
65 valence sulfur species such as  $S_3^-$  and  $S_2^-$  are stable and quite abundant in high temperature  
66 hydrothermal fluids.

67 Sulfur-bearing fluids are often not quenchable, and therefore *in situ* observation at high  
68 pressure and temperature is required to get insight to the prevailing species in the fluid. Raman  
69 spectroscopy has high potential to identify sulfur species, but offers also the option for  
70 quantitative analysis of coexisting species (Binder and Keppler 2011). Often, a hydrothermal  
71 diamond anvil cell was used for *in situ* observation of fluids at elevated pressures and  
72 temperatures (Schmidt 2009; Schmidt and Watenphul 2010; Ni and Keppler 2012). A  
73 disadvantage of this method is that the sample volume is fixed and variation in pressure can be  
74 initiated only indirectly by changing the temperature or the initial load in the sample chamber.  
75 Additionally, low pressures are difficult to adjust properly in such cells, and pressure monitoring  
76 relies on the use of pressure sensors, such as quartz or zircon, that are calibrated for both  
77 pressure and temperature (Schmidt and Ziemann 2000; Schmidt et al. 2013).

78 First optical cells based on sapphire windows have been developed for *in situ* spectroscopy  
79 on fluids at temperatures up to 500°C in the group of Franck in Karlsruhe several decades ago,  
80 see review of Buback et al. (1987). Pressurization was achieved with a hydrothermal fluid which  
81 was separated from the sample fluid by a flexible bellow. Frantz et al. (1993) presented a  
82 miniaturized optical cell for Raman spectroscopy on fluids up to 700 °C and 400 MPa. A  
83 disadvantage was that the sample chamber was directly connected to the pressure medium.  
84 Another type of high-pressure high-temperature setup for *in situ* Raman spectroscopy of  
85 supercritical fluids was reported by Louvel et al. (2015). Sapphire pistons were used for pressure  
86 transfer from the pressure medium helium to a hydrothermal fluid. Based on these experiences,

87 we constructed a new cell allowing for abrupt or continuous changes of pressure at constant  
88 temperature to mimic degassing processes.

89 The high temperature-high pressure application of the cell was tested using solutions of  
90 ammonium sulfate. Ammonium sulfate was selected because of its high solubility in fluids at the  
91  $P$ ,  $T$  conditions of the experiment. Additionally, this solution offers the possibility to study  
92 internal redox reactions initiated by decomposition of ammonium. A further advantage is that  
93 sapphire windows are basically inert against  $(\text{NH}_4)_2\text{SO}_4$  fluids even at the highest  $P$ ,  $T$  conditions  
94 applied.

95

#### 96 THE SPECTROSCOPIC CELL

97 The set up of the new *in situ* Raman spectroscopy pressure cell is shown in Figure 1. The  
98 pressure vessel (1) is machined out of IN 713 LC steel from Doncaster<sup>®</sup>. The material was  
99 already successfully used for cold seal pressure vessels working at temperature/pressure  
100 conditions of 850 °C/500 MPa and 900 °C/100 MPa. An advantage of this material is its low  
101 heat conduction (Zielińska et al. 2010). This minimizes thermal gradients induced by heat  
102 transfer to other components of the cell. The dimensions of the cylindrical cell container are  
103 60 mm in total lengths with an outer diameter of 11.9 mm and inner diameter of 4.5 mm. At the  
104 top, the inner drill hole ends with a conical shape with a total opening angle of 30° over a  
105 distance of 2.8 mm, which acts as the seat for the 2 mm thick polished sapphire or diamond  
106 window. The windows are shaped to have an exact matching angle. At the bottom, the steel body  
107 consists of a screw thread (M16 x 1.5) that fits into a NovaSwiss<sup>®</sup> elbow connector (12). The drill  
108 hole in the lower part of the steel container is extended to 6.5 mm in diameter, with a transition  
109 total angle of 60°. A double-cone (10) with a central drill hole of 1.6 mm is placed between the

110 conical seats of the cell body and the elbow connector for pressure transmittance. To prevent  
111 leakages or any damage (possibly caused by different thermal expansion coefficients of the  
112 materials), the same alloy is used for the vessel and the double cone.

113 To provide chemically inert conditions, the sample fluid is separated from the steel  
114 components by an inlay (3) made of gold tubing with 4.0 mm inner diameter and 0.2 mm  
115 thickness with a tapered top end (30°) and a widened bottom end (60°). A flexible pressure bag  
116 (9) separates the sample fluid from the pressure medium. It is machined from gold tubing with  
117 2.8 mm inner diameter and 0.2 mm thickness using a welded seam or welded gold foil lid (5)  
118 (0.2 mm thickness) as closure on top. The pressure bag is widened with a 60° angle at the bottom  
119 end. The inlay is positioned into the vessel first, followed by the sapphire window and the  
120 pressure bag. The space between window and pressure bag forms the sample chamber. The  
121 pressure vessel is screwed into the NovaSwiss<sup>®</sup> pressure adapter (12) with an open-end wrench  
122 matching the spanner flat (11) until the double cone cold-seals at both ends. The bottom end of  
123 the double cone towards the NovaSwiss<sup>®</sup> adapter has a slightly smaller angle (59°) than the seat  
124 of the connector (60°) to improve sealing.

125

126 **FIGURE 1.** (a) Isometric view of the pressure vessel and heating element. 1 = pressure vessel,  
127 2 = sapphire or diamond window, 3 = inlay (Au), 4 = sample chamber, 5 = welded gold foil lid,  
128 6 = thermocouple, 7 = heating cartridge (brass), 8 = heating wire, 9 = pressure bag (Au),  
129 10 = double-cone, 11 = spanner flat SW11, 12 = NovaSwiss<sup>®</sup> pressure adapter. (b) Technical  
130 drawing of the pressure vessel (1) and the double cone (10) with dimensions in mm. (c) View of  
131 the cell within in the cooling socket and cylindrical cooling box.

132

133 The assembly is mounted on a Carl Zeiss® microscopic adjustment slide, which enables  
134 horizontal positioning of the cell. In order to protect the microscope against heat radiation and  
135 possible release of hot fluid after rupture of cell components, the cell is inserted in a water-  
136 cooled cylindrical box (Fig. 1c). The cooling box is closed with a lid, which contains a 4 mm  
137 diameter hole for the laser to pass. A nitrogen-purged gas-cooling collar helps to further protect  
138 the objective of the microscope against heating.

139 Sapphire was chosen as window material because of good experience in previous *in situ*  
140 spectroscopic studies (e.g. Frantz et al. 1993; Nowak et al. 1996). The window was prepared  
141 from a 2 mm thick disc of a synthetic sapphire crystal orientated parallel to the (001) plane,  
142 which was polished on both sides to finally 0.25 µm. Cylinders with a diameter of 3.9 mm were  
143 drilled from the polished disc, and grinded to a conical shape with a taper of 30°. Sharp edges on  
144 both ends were removed using a diamond file. Finally, the flanks of the cone were polished with  
145 diamond paste down to 1 µm.

146

#### 147 **Pressure control and variation**

148 The pressure is applied by a NovaSwiss® hand pump with a spindle drive using water as  
149 pressure medium. The pump is connected with a flexible pressure tubing (KGT®) to the  
150 spectroscopic cell. Soldered connectors of this tubing limit the pressure to a maximum of  
151 200 MPa. Pressure is measured with a digital WIKA® HP-2 USB pressure transducer with an  
152 uncertainty of 0.25 % in the pressure range of 0 to 200 MPa. The transducer is connected to a PC  
153 and enables to record pressures using the WIKA® communication software EasyCom® 2011.

154 A change in temperature from room temperature to 750 °C at constant pressure of  
155 200 MPa increases the fluid volume by a factor of 2.3, calculated on the basis of pure H<sub>2</sub>O

156 (Wagner and Pruß 2002). Assuming a completely expanded pressure bag at room temperature,  
157 the free fluid volume in the cell is about 70  $\mu\text{l}$ . Thus, the maximum pressure reduction at 750  $^{\circ}\text{C}$   
158 is from 200 MPa to ca. 80 MPa after complete compression of the gold bag. The minimum  
159 pressure, which can be achieved at high temperature, is determined by the initial amount of fluid  
160 and the size of the gold bag. Assuming an initial fluid amount of 35  $\mu\text{l}$  and a corresponding  
161 increase in volume of the pressure bag, the minimum pressure at 750  $^{\circ}\text{C}$  will be 50 MPa. This  
162 simple estimation demonstrates the limits in application of the presented assembly, i.e. pressures  
163 below 50 MPa are extremely difficult to adjust at magmatic temperatures.

164

### 165 **Temperature control and calibration**

166 A standard heating element (HotSet<sup>®</sup> hotslot<sup>®</sup> coil heater, WRP 7803107, 230 V, 225 W,  
167 235 Ohms) mounted on a brass tube was used, limiting the operation temperature to 750  $^{\circ}\text{C}$ . The  
168 heating element is powered by two coupled Delta<sup>®</sup> ES30 (300 V DC, 450 mA, 135 W) current  
169 supplies (regulated in Master/Slave configuration) using a Eurotherm<sup>®</sup> PID controller type 2704f  
170 connected to TC1.

171 Since the temperature inside the cell cannot be directly measured with a thermocouple, the  
172 temperature distribution is externally characterized by (type K) thermocouples in notches on the  
173 micro-vessel at four different distances from the top (TC1 = 5 mm, TC2 = 10 mm, TC3 = 15 mm  
174 and TC4 = 20 mm, compare to Fig. 1b). Temperatures are recorded during the experimental run  
175 with a Mod-Mux module MM8TC combined with the SpecView SCADA Software.

176 The temperature distribution along the cell is shown in Fig. 2a. The difference between  
177 TC1 (Set point temperature of the controller) and TC4 increases from 1  $^{\circ}\text{C}$  at 100  $^{\circ}\text{C}$  (as set  
178 point temperature) to 15  $^{\circ}\text{C}$  at 650  $^{\circ}\text{C}$ . Convection of the fluid is assumed to homogenize

179 efficiently the temperature inside the cell, and thus variation in fluid temperature is expected to  
180 be smaller than measured with the thermocouples. Temperature distribution within the fluid was  
181 determined in a calibration experiment using the Raman shift of the anti-symmetric stretching  
182 mode of zircon  $\nu_3(\text{SiO}_4)$ , which shifts with pressure towards higher wavenumber and with  
183 temperature towards lower wavenumber (Schmidt et al. 2013). The shift of the  $\nu_3(\text{SiO}_4)$  Raman  
184 band at 19 °C induced by a pressure increase from 0.1 MPa to 100 MPa was determined within  
185 the cell to be  $0.73 \pm 0.06 \text{ cm}^{-1}$ . The measured shift is similar to the value of  $0.58 \pm 0.01 \text{ cm}^{-1}/100$   
186 MPa given by Schmidt et al. (2013) for the  $\nu_3(\text{SiO}_4)$  band. Since the pressure range applied in  
187 our study is rather small compared to Schmidt et al. (2013), their determination is considered to  
188 be more precise and, therefore, we applied this value for correcting Raman spectra with respect  
189 to pressure. The corresponding temperatures  $T_{Zr}$  were iteratively determined using the pressure-  
190 corrected values and equation 1 reported in Schmidt et al. (2013):

191

$$192 \quad \nu(\text{cm}^{-1}) = 7.5488 \cdot 10^{-9} \cdot T^3 - 1.6113 \cdot 10^{-5} \cdot T^2 - 2.895 \cdot 10^{-2} \cdot T + 1008.9 \quad (1)$$

193

194 **FIGURE 2.** (a) Temperature distribution in the pressure vessel at 100 °C and 650 °C. TC1-4 refer  
195 to the positions of the thermocouple tips, TC1 represents the set point of the controller. (b)  
196 Comparison of the temperatures measured with thermocouples TC1 and TC2 with  $T_{Zr}$  based on  
197 the Raman shift of the zircon mode  $\nu_3(\text{SiO}_4)$ .

198

199 The precision of equation 1 in terms of wavenumber is better than  $\pm 0.12 \text{ cm}^{-1}$ , depending  
200 on temperature (Schmidt et al. 2013). The uncertainty of the pressure correction is  $\pm 0.01 \text{ cm}^{-1}$   
201  $/100 \text{ MPa}$  (Schmidt et al. 2013). Considering an uncertainty in the determination of the peak

202 position of  $\pm 0.06 \text{ cm}^{-1}$  for the  $\nu_3(\text{SiO}_4)$  band, error propagation leads to a total error of  $\Delta\nu$  of 0.14  
203  $\text{cm}^{-1}$  resulting in an error of the sample temperature of about 4 °C in the range 100 to 700 °C. As  
204 shown in Fig. 2b, the temperature determined using the zircon is lower by 2 °C at 100 °C and by  
205 15 °C at 700 °C than TC1 measured by the thermocouple on top of the cell which was used for  
206 temperature control. On the other hand, temperatures TC2 and TC3 measured in the center of the  
207 cell are in very good agreement with  $T_{Zr}$ . Temperatures given below for the spectra always  
208 represent the corrected temperatures according to  $T_{Zr}$  of this calibration run.

209

210

## EXPERIMENTAL AND ANALYTICS

### 211 **Experimental conditions**

212 A perfect alignment of the sapphire window to the gold plated cone seat (inlay in Fig. 1) of  
213 the pressure vessel is crucial to achieve a good sealing as well as to eliminate any stress on the  
214 window. Even a very small shear stress may produce fractures in the sapphire. Sealing of the  
215 sapphire window is achieved by stepwise “pressure-shooting” at room temperature without a  
216 pressure bag in the cell. In a first step, a pressure of 50 MPa is adjusted in the pressure line  
217 before opening the valve to the vessel. Afterwards, the pressure is progressively increased in  
218 50 MPa steps to 150 MPa. Then, the cell is slowly heated up to 200 °C at a rate of 1 °C/s at  
219 constant volume, means slightly increasing pressure. Finally, the temperature is reduced by 100  
220 °C at a rate of 0.5 °C/s at constant pressure before heating was switched off. This procedure  
221 assured that the window stayed in position while the vessel was shrinking upon cooling. As a  
222 consequence the flanks of the window are pressed into the gold, eliminating any leakage  
223 pathways.

224 After this sealing procedure of the window, the sample chamber was filled with 150 - 200  
225  $\mu\text{l}$  of a 3 molar ammonium sulfate solution ( $(\text{NH}_4)_2\text{SO}_4$  for analysis, EMSURE<sup>®</sup>). The pressure  
226 bag was inserted, pushing out the air and replacing excessive solution. The system is closed by  
227 the double-cone when the pressure vessel is screwed into the pressure adapter. After adjusting  
228 the target pressure, the temperature was increased in steps of 50 °C using a ramp of 1 °C·s<sup>-1</sup>.  
229 Pressure was manually adopted using the spindle drive. Minor changes in the spectra were  
230 observed within the first 5 minutes after adjusting new  $P$ ,  $T$  conditions, probably due to vertical  
231 drifting of the window pushed by thermal expansion of the cell body.

232 The sample chamber volume of the new cell is large compared to diamond anvil cells and  
233 offers sufficient space for placing a capsule next to the pressure bag. The capsule can be used to  
234 add an oxygen or sulfur buffer to the system or to host material for chemical reactions. The setup  
235 of the reaction capsule is illustrated in Fig. 3. Gold tubing of 1.0 mm inner diameter with a wall  
236 thickness of 0.1 mm and a length of 6 - 12 mm was used to prepare the capsule. A mixture of  
237 pyrite and pyrrhotite in mass ratio of 1:1 was used as reactant to test the possible applicability of  
238 the technique to control sulfur fugacity. Corundum was added as a getter to capture iron released  
239 from the reactants.

240 The capsule was welded shut and then pressurized in a cold seal pressure vessel to 30  
241 MPa to compact the assembly. Then, the capsule was pierced at both ends, evacuated and floated  
242 with H<sub>2</sub>O shortly before the experiment. The piercings on top and bottom are large enough to  
243 enable fluid transfer but small enough to prevent transfer of solids into the fluid chamber.

244

245 **FIGURE 3.** Schematic cross section of the reaction capsule. The capsule length is typically ca. 10  
246 mm.

247

## 248 **Raman spectroscopy**

249 Spectra were recorded on a HORIBA Jobin Yvon LabRAM HR 800 UV-Vis Raman  
250 spectrometer using a COBOLT Blues™ DPSS laser with 473 nm wavelengths for excitation.  
251 The CCD-detector offers a resolution of 1024 x 256 pixel and is cooled by a Peltier element.  
252 Unpolarized spectra were acquired in backscattering geometry typically 1000 μm beneath the  
253 window/fluid transition (about 100 μm in the case of window etching) using a 20x magnification  
254 objective with long working distance (N. A. =0.25), a grating of 1800 lines/mm, a focal length of  
255 800 mm and a pinhole of 1000 μm. The measured laser power at the objective was 13 mW.  
256 Accuracy of wavenumber is  $\pm 0.2 \text{ cm}^{-1}$  as determined frequently using a Neon lamp. Spectral  
257 resolution was typically  $0.28 \text{ cm}^{-1}$ . The time for recording a full range spectrum (150 to  $3900 \text{ cm}^{-1}$ )  
258 was 120 s and 320 s depending on accumulation conditions (2 repetitions, 5 s / 10 s  
259 accumulation time).

260 Intensities of recorded Raman spectra were corrected for the response function of the  
261 spectrometer (Frantz et al. 1993). This function was determined by the manufacturer using a  
262 calibrated white light source and corrects for the used excitation wavelength  $\lambda_0$  of the laser and  
263 the grating applied in the measurement.

264

265

## **RESULTS**

### 266 **Redox reactions in ammonium sulfate-bearing fluids**

267 The ability to control temperature and pressure independently offers new possibilities for  
268 *in situ* observations of isobaric or isothermal evolution of fluids using Raman spectroscopy. In  
269 the following sections experiments are presented using 3 molar ammonium sulfate solutions

270 under various conditions. First the sample was heated up to 737 °C while a pressure of 130 MPa  
271 was kept constant. Second the pressure was lowered to 80 MPa while the temperature of 737 °C  
272 was kept constant. At the end the experiment was cooled at 80 MPa pressure to room  
273 temperature. The time span for the experiment was 8 hours in total. Dwells at each step for  
274 measuring spectra were about 10 min.

275 Total intensities of the acquired spectra depend strongly on the parameters used for data  
276 acquisition as well as the position of the volume, which is probed by confocal Raman  
277 spectroscopy. For better comparison of spectral features in Fig. 4, the peak height of the OH  
278 stretching band around 3600 cm<sup>-1</sup> was normalized to 1.

279

280 **FIGURE 4.** Scaled raw data Raman spectra of the isobar heating path in full range and zoomed on  
281 900-1200 cm<sup>-1</sup> and 2200-2700 cm<sup>-1</sup> (a), isothermal decompression path in full range and zoomed  
282 on 1050-1200 cm<sup>-1</sup> and 2200-2700 cm<sup>-1</sup> (b) and isobaric quench path in full range and zoomed on  
283 900-1200 cm<sup>-1</sup> and 2200-2700 cm<sup>-1</sup> (c). Signals at 416 cm<sup>-1</sup> (strong), 576 cm<sup>-1</sup> (medium) and 749  
284 cm<sup>-1</sup> (medium) are caused by the sapphire window.

285

286 **TABLE 1.** Raman frequencies above 900 cm<sup>-1</sup> and species assignments.

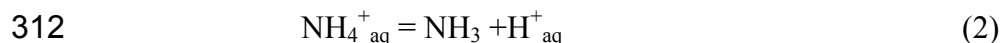
287

288 **Isobaric heating.** Raman spectra recorded during heating at 130 MPa fluid pressure are  
289 shown in Figure 4a. Detailed band assignment is given in Table 1. Dominating features at 22 °C  
290 are the very intensive and narrow peak at 980 cm<sup>-1</sup> assigned to SO<sub>4</sub><sup>2-</sup> (Rudolph 1996; Schmidt  
291 2009) and the broad, asymmetric OH stretching vibration band of water molecules with  
292 maximum at 3443 cm<sup>-1</sup> (Schmidt and Watenphul 2010; Schmidt and Manning 2017).

293 Superimposed on the low-wavenumber tail of this band at 3000-3200  $\text{cm}^{-1}$  are bands of the NH  
294 stretching-vibration of ammonium ions (Schmidt and Watenphul 2010; Schmidt and Manning  
295 2017). The OH-NH band system is strongly affected by hydrogen bonding. With increasing  
296 temperature at constant pressure, fluid density decreases and, as a consequence, hydrogen  
297 bonding is reduced (e.g. Soper 2000; Sahle et al. 2013). Thus, the OH and NH related peaks are  
298 getting narrower and shift towards higher wavenumber. At temperatures above 191 °C up to 489  
299 °C, spectra were strongly affected by fluorescence superimposing the Raman signal, probably  
300 due to contamination by organic material during set-up of the cell. An indication for such  
301 contamination is the additional small signal at 2830  $\text{cm}^{-1}$ , possibly originating from CH -  
302 vibrations. Within this temperature region the signal of  $\text{SO}_4^{2-}$  decreases and a new band forms at  
303 1050  $\text{cm}^{-1}$ , assigned to  $\text{HSO}_4^-$  (Rudolph 1996). While the shape of the  $\text{SO}_4^{2-}$  band appears  
304 symmetric the  $\text{HSO}_4^-$  band has an asymmetry towards lower wavenumber. At 489 °C,  $\text{SO}_4^{2-}$  is  
305 still observed in the fluid while the intensity of  $\text{HSO}_4^-$  increases. At 1140  $\text{cm}^{-1}$ , a new peak  
306 appears, which has been interpreted as overlapping signals of  $\text{H}_2\text{SO}_4$  ( $\sim 1140 \text{ cm}^{-1}$ ) and  $\text{SO}_2$   
307 ( $1145 \text{ cm}^{-1}$ ) in previous studies (Walrafen 1964; Maillard et al. 1975; Ni and Keppler 2012). The  
308  $\text{HSO}_4^-$  signal vanished at 685 °C, and the band system near 1140  $\text{cm}^{-1}$  represents the only  
309 remaining sulfate species.

310 Two narrow peaks at 3233 and 3314  $\text{cm}^{-1}$  are firstly observed at 339 °C during heating.

311 The peaks are assigned to  $\text{NH}_3$  (Buback and Schulz 1976) formed by the dissociation reaction



313 where the subscript *aq* indicates that these species are stabilized in aqueous complexes. The  
314 dissociation is a consequence of decreasing hydrogen bonding with increasing temperature. At  
315 the highest temperature of 737 °C NH and OH related peaks are well separated in the spectra.

316 A sharp signal at  $2323\text{ cm}^{-1}$  appears at  $591\text{ }^{\circ}\text{C}$ , increasing with temperature. This signal  
317 was assigned to  $\text{N}_2$  (Schroetter and Kloeckner 1979), formed by decomposition of  $\text{NH}_3$ . At  $737$   
318  $^{\circ}\text{C}$ , the  $1140\text{ cm}^{-1}$  band system decreases in intensity, and a new signal around  $2580\text{ cm}^{-1}$  is  
319 visible, which is composed by a weak signal at  $2578\text{ cm}^{-1}$  assigned to  $\text{HS}^-$  and a stronger signal at  
320  $2590\text{ cm}^{-1}$  assigned to  $\text{H}_2\text{S}$  (Rosasco and Roedder 1979; Bény et al. 1982; Chazallon et al. 2007).

321

322 **Isothermal decompression.** Fig. 4b illustrates the evolution of the Raman spectra upon  
323 decompression from  $130\text{ MPa}$  to  $80\text{ MPa}$  at  $737\text{ }^{\circ}\text{C}$ . In this pressure range, in the case of pure  
324 water, the density is supposed to decrease by a factor of 1.6 from  $0.34\text{ g/cm}^3$  to  $0.21\text{ g/cm}^3$   
325 (Wagner and Pruß 2002). The response of Raman spectra to pressure changes is very fast, i.e.  
326 stable conditions were achieved two minutes after pressure drop.

327 There are not many changes in the spectra after decompression. The sulfate-related bands  
328 near  $1140\text{ cm}^{-1}$  and  $\text{NH}_3$ -related signals near  $3200\text{ cm}^{-1}$  slightly decrease in intensity compared to  
329 the OH bands, whereas the peaks assigned to  $\text{N}_2$  and  $\text{HS}^-/\text{H}_2\text{S}$  slightly increase. The latter trend  
330 suggests continuation of the internal reduction reaction in the fluid during decompression.

331

332 **Isobaric cooling.** To test the reversibility of effects observed during heating, Raman  
333 spectra were collected during isobaric cooling at  $80\text{ MPa}$  (Fig. 4c). Below  $343\text{ }^{\circ}\text{C}$  spectra were  
334 very noisy and the background increased, i.e. in the low and in the high wavenumber range, and  
335 even qualitative statements about peak evolutions were not possible. Thus, we could not re-  
336 measure the fluid after the run at ambient temperature.

337 Towards low temperatures, intensities of all signals are slightly increasing. Sulfate-related  
338 peaks show the same trend as observed during heating, i.e. an increasing stability of ionic species

339 towards lower temperature from  $\text{H}_2\text{SO}_4$  to  $\text{HSO}_4^-$  to  $\text{SO}_4^{2-}$ .  $\text{HSO}_4^-$  was firstly observed at 489 °C  
340 and  $\text{SO}_4^{2-}$  at 388 °C (see inlet in Fig. 4c). These temperatures are roughly consistent with the  
341 heating path although confining pressure was different. The signals of  $\text{HS}^-/\text{H}_2\text{S}$  and  $\text{N}_2$  are  
342 visible in all spectra (see inlet in Fig. 4c). While the intensity of the  $\text{HS}^-/\text{H}_2\text{S}$  remains roughly  
343 constant over the whole temperature range, the intensity of the  $\text{N}_2$  peak is continuously  
344 increasing. The  $\text{NH}_3$  bands decrease during cooling but re-formation of the  $\text{NH}_4^+$ -related bands  
345 during cooling cannot be approved due to the increase in background. Although a final proof is  
346 missing, a reversibility of reaction (2) is very likely on the basis of the observations. On the other  
347 hand, it is evident that the reduction of sulfate species to sulfide species is irreversible.

348

#### 349 **Fluid-Solid interaction**

350 The experiment with 3 molar ammonium sulfate solution and a reaction capsule  
351 containing a pyrrhotite/pyrite mixture was also affected by fluorescence at low temperatures, and  
352 Raman spectra could be recorded during heating only above 500 °C (Fig. 5a). During cooling the  
353 whole temperature range was accessible down to room temperature (Fig. 5b).

354

355 **FIGURE 5.** (a) Raman spectra recorded on ammonium sulfate solutions in contact with  
356 pyrite/pyrrhotite mixture at constant pressure of 130 MPa and temperatures of 592-685 °C during  
357 heating. For comparison the spectrum of the experiment without pyrite/pyrrhotite at 685 °C is  
358 shown. (b) Evolution of spectra during cooling to room pressure at same pressure.

359

360 The evolution of spectra during heating is similar as in the experiment without reaction  
361 capsule except that the  $\text{HS}^-/\text{H}_2\text{S}$  band system was firstly observed at much lower temperature of

362 592 °C (Fig. 5a). Additionally, the high temperature spectra in presence of pyrite/pyrrhotite show  
363 a pronounced peak at 567 cm<sup>-1</sup>, which appears to be correlated in intensity to the HS<sup>-</sup>/H<sub>2</sub>S band  
364 system. Duration of the heating path was similar in both experiments.

365 During cooling, the evolution of sulfate-related bands is similar to the experiment without  
366 sulfur-bearing minerals (Fig. 5b). The H<sub>2</sub>SO<sub>4</sub> band system near 1140 cm<sup>-1</sup> disappeared at 400 °C;  
367 HSO<sub>4</sub><sup>-</sup> was firstly observed at 489 °C and disappeared at 191 °C; SO<sub>4</sub><sup>2-</sup> was firstly visible in the  
368 spectrum recorded at 391 °C. The N<sub>2</sub> peak is much more pronounced than in the  
369 pyrrhotite/pyrite-free experiments, and the HS<sup>-</sup>/H<sub>2</sub>S band system is visible even at room  
370 temperature after cooling. Below 200 °C the H<sub>2</sub>S component systematically decreases and in the  
371 r.t. spectrum only HS<sup>-</sup> is present. Again, this observation is in line with stabilization of ionic  
372 species by aqua complexes at low *T* and high fluid density.

373 In the low wavenumber range, some distinct differences to Fig. 4 need to be  
374 acknowledged. At 685 °C an intense peak occurs at 567 cm<sup>-1</sup> concomitant with growth of the HS<sup>-</sup>  
375 /H<sub>2</sub>S band (Fig. 5a). Upon cooling, this band is dramatically reduced in intensity already at 591  
376 °C (Fig. 5b), indicating that the responsible species is highly *P*, *T* dependent. The absence of this  
377 peak in the system without reaction capsule (Fig. 4) suggests that the 567 cm<sup>-1</sup> peak relies on  
378 specific conditions induced by the pyrrhotite/pyrite assemblage. It is very likely that this band is  
379 caused by S<sup>2-</sup> ions in the fluid (Pokrovski and Dubessy 2015; Schmidt and Seward 2017).

380 Another intense peak is formed at 527 cm<sup>-1</sup> at intermediate temperatures and disappeared  
381 below 200 °C. According to Pokrovski and Dubessy (2015), this band can be assigned to the  
382 symmetric stretching vibration of the S<sub>3</sub><sup>-</sup> ion that forms in solutions in which sulfate and sulfide  
383 coexist. The large shoulder at the HSO<sub>4</sub><sup>-</sup> peak at 1060 cm<sup>-1</sup> is due to the 2<sup>nd</sup> order harmonics of  
384 the S<sub>3</sub><sup>-</sup> that exhibits a resonance phenomenon at the applied laser wavelength (Pokrovski, pers.

385 communication). The large and multiple peak feature clearly apparent in the 295 °C spectrum  
386 around 450 cm<sup>-1</sup> in Fig. 5b is likely to be polymeric molecular sulfur in solution (Pokrovski and  
387 Dubessy 2015; Barré et al. 2017).

388 Microscopic investigation on a polished cross section of the reaction capsule after the run  
389 gives evidence for proceeding reactions in the mineral assemblage. A porous layer was formed  
390 around large pyrrhotite grains. The newly formed phase was identified as pyrite by Raman  
391 spectroscopy. Thus, oxidation of sulfide is evident in the powder, most likely by sulfate from the  
392 fluid. Outside the reaction capsule, sulfate was still present in large concentration and sulfide was  
393 formed by homogeneous redox reaction in the fluid. These findings suggest that the capsule  
394 interior and the fluid outside the capsule were not in chemical equilibrium.

395

396

## DISCUSSION

### 397 Fitting of band components and intensity corrections

398 In order to analyze changes in abundance of species during the experiment, we  
399 deconvoluted the Raman spectra. Spectra were fitted with a minimum number of Pseudo-Voigt  
400 functions required to reproduce the measured spectrum in the respective ranges of interest. All  
401 bands are consistent with band assignments for given species as outlined above. The Pseudo-  
402 Voigt function was based on the normalized sum of a Gaussian and a Lorentzian. The Gauss-  
403 Lorentz ratio was constrained to be the same for all fitted peaks within a given subrange. Broad  
404 and asymmetric band systems like the OH band system were fitted by several peaks to describe  
405 the envelope of the band system. Individual peaks have no direct meaning and are only used to  
406 determine the intensity of the band system. During the fit of these individual spectral regions of  
407 interest, we used linear baselines for simplicity. Ranges of particular interests are at 950 - 1200

408  $\text{cm}^{-1}$ , where different sulfate species and possibly  $\text{SO}_2$  occur, at  $2300 - 2600 \text{ cm}^{-1}$ , where  
409 vibrations of  $\text{N}_2$  and  $\text{HS}^-/\text{H}_2\text{S}$  are excited, and  $2600 - 3800 \text{ cm}^{-1}$ , which is the range of OH and  
410 NH stretching vibrations.

411

412 **FIGURE 6.** Deconvolution of Raman signals in selected spectral regions for the experiment with 3  
413 molar ammonium sulfate solution at different P, T conditions. For band assignment see Table 1.  
414 (a) - (c) Regime of OH and NH stretching vibrations. (d) - (f) Regime of  $\text{H}_2\text{SO}_4$  stretching  
415 vibrations. (g) - (h) Regime of SH stretching vibrations.

416

417 The broad band system of the ammonium sulfate solution at  $2600 - 3800 \text{ cm}^{-1}$  measured at  
418  $20 \text{ }^\circ\text{C}$ ,  $130 \text{ MPa}$  can be reproduced well using five components, the three high frequency bands  
419 are assigned to OH stretching vibration bands of water molecules and the two bands at lower  
420 frequency ( $2930$  and  $3073 \text{ cm}^{-1}$ ) are assigned to NH stretching vibrations of  $\text{NH}_4^+$  ions (Fig. 6a).  
421 Ammonium ions are only a minor species at  $600 \text{ }^\circ\text{C}$  and are absent at  $734 \text{ }^\circ\text{C}$  (Fig. 6b,c). Instead  
422 of that, well-resolved bands of  $\text{NH}_3$  occur in the high temperature spectra at  $3232$  and  $3322 \text{ cm}^{-1}$ .

423 Simultaneously with the disappearance of the  $\text{NH}_4^+$  species, sulfate groups are transformed  
424 first to  $\text{HSO}_4^-$  and then to  $\text{H}_2\text{SO}_4$  units. The evolution of the latter band system located around  
425  $1140 \text{ cm}^{-1}$  is shown in Figure 6d-f. Three band components are sufficient to fit the spectra in this  
426 region, the broad additional component in Figure 6f can be considered as being part of the  
427 background. A key question is whether the narrow band component at  $1145 \text{ cm}^{-1}$  is caused by  
428 symmetrical stretching vibration of  $\text{SO}_2$  molecules (Maillard et al. 1975; Ni and Keppler 2012).  
429 Ni and Keppler (2012) made such assignment in their *in situ* Raman study on sulfuric acid at  
430 temperatures up to  $700 \text{ }^\circ\text{C}$ . A possible explanation given by the authors is that the solution

431 reacted with rhenium metal from the gasket of the diamond anvil cell, as indicated by the  
432 observation of rhenium oxide in the assembly after experiment.

433 We have several reasons inferring that this is not the case in our experiments: (i) The  
434 intensity ratio of sub-bands in this region depends only weakly on temperature and pressure, and  
435 we do not observe a systematic relative increase of the  $1145\text{ cm}^{-1}$  component with dwell time at  
436 high temperature. Such trend would be expected for a progressing reduction reaction in the fluid  
437 that produces sulfur dioxide. (ii) The  $1145\text{ cm}^{-1}$  band completely vanished during cooling  
438 together with the other band components in this spectral region. In the study of Ni and Keppler  
439 (2012) the  $\text{SO}_2$  peak was still present in the post-experimental spectra recorded at room  
440 temperature. (iii) The degradation of the band system at  $1140\text{ cm}^{-1}$  and the formation of the band  
441 system at  $1040\text{ cm}^{-1}$  during cooling occurs very fast (Fig. 4c). This trend is consistent with rapid  
442 protonation/deprotonation processes but not with complex redox reactions, which are typically  
443 slow. Thus, we assign the band at  $1145\text{ cm}^{-1}$  to a symmetrical  $\text{SO}_2$  stretching vibration in  $\text{H}_2\text{SO}_4$   
444 molecules, denoted in following as  $^*\text{H}_2\text{SO}_4$ .

445 A major difference of our spectra above  $600\text{ }^\circ\text{C}$  to those of sulfuric acid shown in Ni and  
446 Keppler (2012) is the absence of the band at  $1200\text{ cm}^{-1}$ , assigned to the  $\nu_1$  mode of  $\text{H}_2\text{SO}_4$  by  
447 these authors. We attribute the different findings to the composition of the fluid, i.e. the presence  
448 of ammonium. A strong change in fluid properties after addition of ammonium can be inferred  
449 from experiments of Schmidt and Watenphul (2010). They observed a drastic decrease of silica  
450 solubility for  $\text{NH}_4\text{Cl}$ -bearing solutions compared to a pure  $\text{H}_2\text{O}$  fluid, e.g. by a factor of 2 at  
451  $500^\circ\text{C}$ ,  $500\text{ MPa}$  for a  $6.6\text{ m NH}_4\text{Cl}$  solution. These observations indicate that dissolved  
452 ammonium reduces the capability of fluids to form solvation complexes. Thus,  $^*\text{H}_2\text{SO}_4$  most

453 likely represents a state with very weak to negligible interaction with neighboring fluid  
454 constituents.

455 The band system at  $2580\text{ cm}^{-1}$  can be fitted by three components. The two components at  
456 higher wavenumber are assigned to  $\text{H}_2\text{S}$  molecules and the broader one at lower wavenumber to  
457  $\text{HS}^-$  ions (Table 1). Both species coexist down to temperatures of  $200\text{ }^\circ\text{C}$  (Fig. 5b), at lower  
458 temperatures the high-wavenumber components systematically decrease in abundance, and  $\text{HS}^-$   
459 appears to be the only sulfide species in solution at room temperature.

460

### 461 **Evolution of species abundance with temperature and pressure**

462 Peak areas determined by fitting the spectra as described above were used to monitor the  
463 evolution of species abundance during the experiments. Using the position of peak maxima, peak  
464 areas were corrected for the temperature dependence of Stoke's scattering cross section  
465 according to (Long 1977; Rudolph and Irmer 2007):

$$466 \quad F_{BE} = \frac{1}{1 - \exp\left(\frac{-hc\omega_j}{k_B T}\right)} \quad (3)$$

467 where  $h$  is Planck's constant,  $c$  the speed of light,  $\omega_j$  the Raman shift (peak position),  $k_B$  the  
468 Boltzmann constant and  $T$  the absolute temperature. The wavenumber dependence of the Raman  
469 scattering intensity was considered according to (Rudolph and Irmer 2007) by dividing with a  
470 factor

$$471 \quad F_s = (\omega_0 - \omega_j)^3 \omega_j^{-1} \quad (4)$$

472 where  $\omega_0$  is the wavenumber of the exciting light. Scaling of the intensity of a given species to  
473 the total peak area of the OH vibration bands was used to reduce effects induced by changing  
474 temperature and pressure of the fluid (Schmidt 2009; Schmidt and Manning 2017). Thus, a

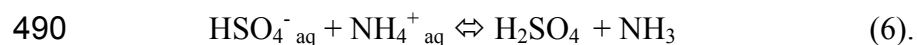
475 qualitative description of species evolution during the experiment was achieved. Quantification  
476 suffers from missing knowledge of Raman cross section for the bands. Raman cross sections  
477 may strongly change from band to band, and are expected to be highly dependent on fluid  
478 properties. Errors in normalized intensities were estimated from counting statistics.

479

480 **FIGURE 7.** Evolution of species abundance during (a) heating, (b) decompression and (c)  
481 cooling. Peak areas are normalized to the area of the total OH signals. \*H<sub>2</sub>SO<sub>4</sub> refers to the band  
482 at 1145 cm<sup>-1</sup>, which has been assigned to SO<sub>2</sub> molecules in previous study. Error bars are not  
483 shown for clarity. Errors are smaller than the symbols for values ≥ 0.0005.

484

485 **Homogeneous reaction.** Fig. 7 shows the results obtained for the experiment with the  
486 ammonium sulfate solution. As a general trend highly charged ions are stable only in high  
487 density fluids while in low-density fluids molecular species are predominant. In the case of the  
488 ammonium sulfate solution, these trends can be described by the following reactions



491 During cooling the backwards reaction, i.e. formation of ionic species, is shifted to lower  
492 temperatures (Fig. 7c) due to lower pressure and hence lower fluid density. For instance, at 500  
493 °C and 80 MPa, when HSO<sub>4</sub><sup>-</sup> re-appears during cooling, the density of pure H<sub>2</sub>O fluid would be  
494 0.46 g/cm<sup>3</sup> at these conditions (Wagner and Pruß 2002). The same density at 130 MPa would be  
495 reached at 600 °C.

496 The appearance of the N<sub>2</sub> signal at 586 °C indicates the onset of redox reactions in the  
497 fluid. Evidence for reduction of sulfate is given by occurrence of the band system at 2580 cm<sup>-1</sup> at  
498 high temperature. H<sub>2</sub>S coexists with HS<sup>-</sup>, which may be described by



500 Neither decompression nor quench leads to a re-oxidation of HS<sup>-</sup>/H<sub>2</sub>S. Thus, it seems, once  
501 formed, sulfide species remain stable under prevalent conditions. As noted above, despite of the  
502 occurrence of a peak at 1145 cm<sup>-1</sup>, we don't see an indication for the formation of SO<sub>2</sub>, in  
503 contrary to Ni and Keppler (2012). Roughly parallel trends for H<sub>2</sub>SO<sub>4</sub> (sum of areas of sub-bands  
504 at 1131 and 1138 cm<sup>-1</sup>) and \*H<sub>2</sub>SO<sub>4</sub> (areas of sub-band at 1145 cm<sup>-1</sup>) also support this statement.  
505 The reason for the different findings in Ni and Keppler (2012) is probably the oxygen fugacity in  
506 the experiments. Ni and Keppler (2012) detected rhenium oxide in the sample after experiment  
507 and suggest that conditions were probably close to the Re-ReO<sub>2</sub> oxygen buffer. Using  
508 thermodynamic data of Pownceby and O'Neill (1994) and assuming for simplicity ideal mixing  
509 in the fluid, the corresponding hydrogen fugacity at 700 °C/130 MPa is about 0.05 MPa.  
510 Decomposition of 0.2% of the loaded ammonium sulfate would be sufficient to generate such  
511 hydrogen pressure, if hydrogen is not consumed by subsequent reactions. Comparing the area of  
512 NH<sub>3</sub>-related bands of the heating path with the cooling path implies that 20% of NH<sub>3</sub> was  
513 converted to nitrogen and hydrogen, supporting the hypothesis of a much lower oxygen fugacity  
514 in our system compared to Ni and Keppler (2012). However, pressures were different during  
515 heating and cooling and Raman cross-sections of the bands are not known so that we cannot  
516 make quantitative statements about the extent of the redox reaction.

517 Due to experimental failure we could not collect spectra at the end of the experiment and,  
518 hence, the degree of the dissociation of ammonium could not be determined. Comparing NH<sub>3</sub>-

519 related peaks at 489 °C during heating and cooling implies that more than 90% of NH<sub>3</sub> survived  
520 the high temperature treatment (Fig. 7a,c). But due to different pressures and probably different  
521 NH<sub>3</sub>/NH<sub>4</sub><sup>+</sup> ratios this value is not more than a rough estimate.

522

523 **FIGURE 8.** Species evolution during (a) heating and (b) cooling in presence of a pyrrhotite/pyrite  
524 assembly. Peak areas are normalized to the area of the total OH signals. \*H<sub>2</sub>SO<sub>4</sub> refers to the  
525 band at 1145 cm<sup>-1</sup>, which has been assigned to SO<sub>2</sub> molecules in previous study. Error bars are  
526 not shown for clarity.

527

528 **Heterogeneous reaction.** For the experiment with the pyrrhotite/pyrite capsule,  
529 comparison of NH<sub>4</sub><sup>+</sup>-related bands at room temperature before and after experiment indicate that  
530 50% of the ammonium has reacted (Fig. 8a,b). H<sub>2</sub>S formation in the fluid was negligible below  
531 592 °C. In the interval 592 °C → 685 °C → 592 °C the area ratio for the sum of HS<sup>-</sup> + H<sub>2</sub>S peaks  
532 increases by a factor of four from 0.0021 to 0.0092. An even larger increase from 0.0003 to  
533 0.0037 occurs for the N<sub>2</sub> band during this cycle. This implies that a large fraction of the sulfide  
534 species in the fluid was formed by reduction of sulfate with hydrogen originating from  
535 decomposition of NH<sub>3</sub>. However, we cannot completely exclude some contribution by  
536 dissolution of pyrrhotite inside the reaction capsule and transport of dissolved species outwards.  
537 On the other hand, Figure 6 shows that pyrrhotite is covered by pyrite and release of FeS is  
538 increasingly hindered with progressing reaction. The reaction products are highly porous, which  
539 may indicate a volume reduction of solids during reaction.

540 The apparent disequilibrium between the fluid phase inside and outside the reaction  
541 capsule points to kinetic barriers in the system. Limiting parameters are the reaction kinetics of

542 transformation of pyrrhotite to pyrite as well as fluid transport in the pore system within the  
543 capsule but possibly also reactions between fluid components (e.g. iron released from the sulfur-  
544 bearing minerals) and corundum of the window. Such kinetic problems will also limit the  
545 possibility to use a reaction capsule to control oxygen fugacity in the spectroscopic cell. Only if  
546 the initial conditions in the fluid are close to the equilibrium conditions imposed by the solid  
547 buffer system, the exchange between capsule interior and outside fluid will be sufficient to  
548 maintain equilibrium on the time scale of hours, which is the accessible working time for the  
549 spectroscopic cell.

550

551

### IMPLICATIONS

552 The new spectroscopic cell developed in this study allows observation of hydrothermal  
553 and magmatic fluids at temperatures up to 750 °C and pressures up to 200 MPa. Pressure and  
554 temperature can be independently varied and thus, enables simulation of decompression of fluids  
555 during ascent in the Earth's crust. The cell has sufficient space inside to add a small capsule to  
556 study interaction of fluids with solid materials. This assembly may be used to control sulfur  
557 and/or oxygen fugacity in the fluid. However, mass transfer between the capsule and duration of  
558 the high  $T$  experiments is limited so that equilibrium conditions can be adjusted only for specific  
559 conditions.

560 Combining the cell with Raman spectroscopy is a powerful method to study  
561 homogeneous reactions in fluids with high temporal resolution, depending mainly on the  
562 available Raman spectrometer. Tests on 3 molar ammonium sulfate solutions demonstrate the  
563 importance of fluid density for stabilization of ionic species. Ammonium was found to have high

564 thermal stability under conditions of the Earth's crust. Even at temperatures of 700 °C in  
565 presence of an oxidant, the lifetime of NH<sub>3</sub> is at least several hours.

566 The experiments performed in our studies have also implications concerning the  
567 evolution of sulfur species during degassing of magmas and subsequent ascent of fluids to the  
568 Earth's surface. Formation of SO<sub>2</sub> in sulfate-bearing fluids, as observed in the study of Ni and  
569 Keppler (2012), seems to depend strongly on the prevailing redox conditions in the system. In  
570 presence of strongly reducing agents (such as ammonium) sulfide species will be formed while at  
571 moderate redox conditions, SO<sub>2</sub> is the reaction product. Confining pressure will also play a  
572 crucial role for the reaction.

573

574

#### ACKNOWLEDGEMENTS

575 This work was supported by the German Science Foundation (DFG grants BE 1720/35  
576 and SCHM 2415/3). A synthetic sapphire crystal was kindly provided by R. Uecker from IKZ  
577 Berlin; a natural non-metamict zircon used for pressure calibration is a donation of T. Geisler-  
578 Wierwille, Bonn. The authors want to thank the workshop crew of the Helmholtz Centre  
579 Potsdam as well as the workshop crew at the Institute of Mineralogy at Leibniz Universität  
580 Hannover for technical support. Special thanks to Christian Schmidt for support during Raman  
581 measurements. Helpful comments by Yann Morizet, Gleb Pokrovski and an anonymous reviewer  
582 are acknowledged.

583

584

585

586

587

## REFERENCES

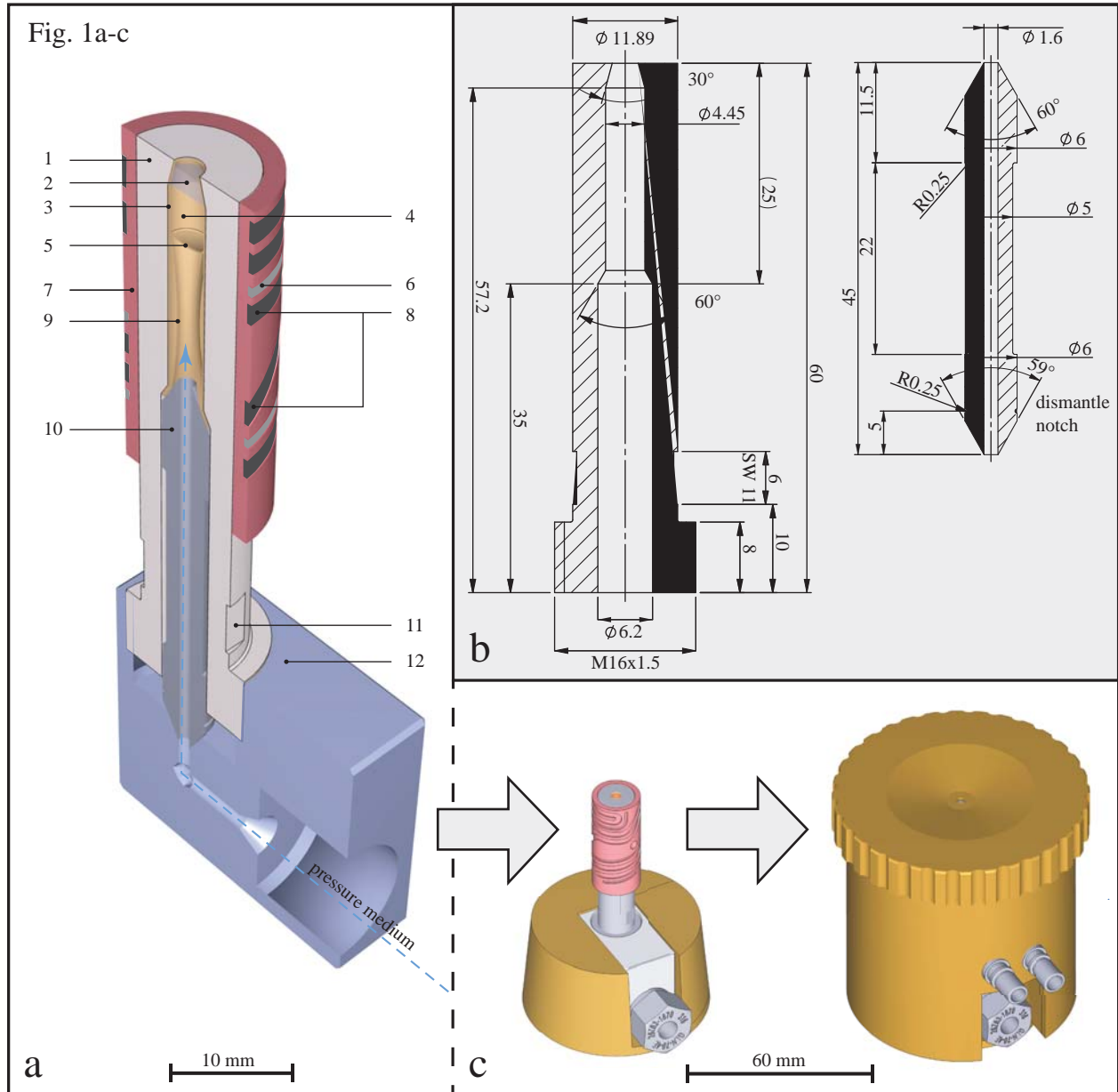
- 588 Barré, G., Truche, L., Bazarkina, E.F., Michels, R., and Dubessy, J. (2017) First evidence of the  
589 trisulfur radical ion  $S_3^-$  and other sulfur polymers in natural fluid inclusions. *Chemical*  
590 *Geology*, 462, 1–14.
- 591 Bény, C., Guilhaumou, N., and Touray, J.-C. (1982) Native-sulphur-bearing fluid inclusions in  
592 the  $CO_2$ - $H_2S$ -S system - microthermometry and Raman microprobe (mole) analysis -  
593 thermochemical interpretations. *Chemical Geology*, 37, 113–127.
- 594 Binder, B., and Keppler, H. (2011) The oxidation state of sulfur in magmatic fluids. *Earth and*  
595 *Planetary Science Letters*, 301, 190–198.
- 596 Buback, M., and Schulz, K.R. (1976) Raman scattering of pure ammonia at high pressures and  
597 temperatures. *The Journal of Physical Chemistry*, 80, 2478–2482.
- 598 Buback, M., Crerar, D.A., and Vogel Koplitz, L.M. (1987) Vibrational and Electronic  
599 Spectroscopy of Hydrothermal Systems, 333-359 p.
- 600 Burgisser, A., Poussineau, S., Arbaret, L., Druitt, T.H., Giachetti, T., and Bourdier, J.-L. (2010)  
601 Pre-explosive conduit conditions of the 1997 Vulcanian explosions at Soufrière Hills  
602 Volcano, Montserrat: I. Pressure and vesicularity distributions. *Journal of Volcanology and*  
603 *Geothermal Research*, 194, 27–41.
- 604 Burgisser, A., Arbaret, L., Druitt, T.H., and Giachetti, T. (2011) Pre-explosive conduit conditions  
605 of the 1997 Vulcanian explosions at Soufrière Hills Volcano, Montserrat: II. Overpressure  
606 and depth distributions. *Journal of Volcanology and Geothermal Research*, 199, 193–205.
- 607 Chazallon, B., Focsa, C., Charlou, J., and Bourry, C. (2007) A comparative Raman spectroscopic  
608 study of natural gas hydrates collected at different geological sites. *Chemical Geology*, 244,  
609 175–185.

- 610 de Moor, J.M., Fischer, T.P., Sharp, Z.D., King, P.L., Wilke, M., Botcharnikov, R.E., Cottrell,  
611 E., Zelenski, M., Marty, B., Klimm, K., and others (2013) Sulfur degassing at Erta Ale  
612 (Ethiopia) and Masaya (Nicaragua) volcanoes: Implications for degassing processes and  
613 oxygen fugacities of basaltic systems. *Geochemistry, Geophysics, Geosystems*, 14, 4076–  
614 4108.
- 615 Frantz, J.D., Dubessy, J., and Mysen, B. (1993) An optical cell for Raman spectroscopic studies  
616 of supercritical fluids and its application to the study of water to 500°C and 2000 bar.  
617 *Chemical geology*, 106, 9–26.
- 618 Long, D.A. (1977) *Raman Spectroscopy*, 276 p. McGraw-Hill Vol. 2. McGraw-Hill.
- 619 Louvel, M., Bordage, A., Da Silva-Cadoux, C., Testemale, D., Lahera, E., Del Net, W.,  
620 Geaymond, O., Dubessy, J., Argoud, R., and Hazemann, J. (2015) A high-pressure high-  
621 temperature setup for in situ Raman spectroscopy of supercritical fluids. *Journal of*  
622 *Molecular Liquids*, 205, 54–60.
- 623 Maillard, D., Allavena, M., and Perchard, J.P. (1975) Spectres vibrationnels du dioxyde de  
624 soufre dans une matrice d'argon, d'azote et de xénon. *Spectrochimica Acta*, 31A, 1523–  
625 1531.
- 626 Müller-Simon, H. (2011) Fining of Glass Melts. *Reviews in Mineralogy and Geochemistry*, 73,  
627 337–361.
- 628 Ni, H., and Keppler, H. (2012) In-situ Raman spectroscopic study of sulfur speciation in  
629 oxidized magmatic-hydrothermal fluids. *American Mineralogist*, 97, 1348–1353.
- 630 Nowak, M., Behrens, H., and Johannes, W. (1996) A new type of high-temperature, high-  
631 pressure cell for spectroscopic studies of hydrous silicate melts. *American Mineralogist*, 81,  
632 1507–1512.

- 633 Pokrovski, G.S., and Dubessy, J. (2015) Stability and abundance of the trisulfur radical ion  $S_3^-$  in  
634 hydrothermal fluids. *Earth and Planetary Science Letters*, 411, 298–309.
- 635 Pokrovski, G.S., and Dubrovinsky, L.S. (2011) The  $S_3^-$  ion is stable in geological fluids at  
636 elevated temperatures and pressures. *Science (New York, N.Y.)*, 331, 1052–4.
- 637 Pokrovski, G.S., Borisova, A.Y., and Harrichoury, J.C. (2008) The effect of sulfur on vapor-  
638 liquid fractionation of metals in hydrothermal systems. *Earth and Planetary Science Letters*,  
639 266, 345–362.
- 640 Pownceby, M.I., and O'Neill, H.S.C. (1994) Thermodynamic data from redox reactions at high  
641 temperatures . IV . Calibration of the Re-ReO<sub>2</sub> oxygen buffer from EMF and NiO + Ni-Pd  
642 redox sensor measurements. *Contributions to Mineralogy and Petrology*, 2, 130–137.
- 643 Rosasco, G.J., and Roedder, E. (1979) Application of a new Raman microprobe spectrometer to  
644 nondestructive analysis of sulfate and other ions in individual phases in fluid inclusions in  
645 minerals. *Geochimica et Cosmochimica Acta*, 43, 1907–1915.
- 646 Rudolph, W. (1996) Structure and dissociation of the hydrogen sulphate ion in aqueous solution  
647 over a broad temperature range: a Raman study. *Zeitschrift für Physikalische Chemie*, 194,  
648 73–95.
- 649 Rudolph, W.W., and Irmer, G. (2007) Raman and infrared spectroscopic investigations on  
650 aqueous alkali metal phosphate solutions and density functional theory calculations of  
651 phosphate-water clusters. *Applied Spectroscopy*, 61, 1312–1327.
- 652 Sahle, C.J., Sternemann, C., Schmidt, C., Lehtola, S., Jahn, S., Simonelli, L., Huotari, S., Hakala,  
653 M., Pylkkanen, T., Nyrow, A., and others (2013) Microscopic structure of water at elevated  
654 pressures and temperatures. *Proceedings of the National Academy of Sciences*, 110, 6301–  
655 6306.

- 656 Schmidt, C. (2009) Raman spectroscopic study of a H<sub>2</sub>O+Na<sub>2</sub>SO<sub>4</sub> solution at 21–600°C and  
657 0.1MPa to 1.1GPa: Relative differential  $\nu_1$ -SO<sub>4</sub><sup>2-</sup> Raman scattering cross sections and  
658 evidence of the liquid–liquid transition. *Geochimica et Cosmochimica Acta*, 73, 425–437.
- 659 Schmidt, C., and Manning, C.E. (2017) Pressure-induced ion pairing in MgSO<sub>4</sub> solutions:  
660 Implications for the oceans of icy worlds. *Geochemical Perspectives Letters*, 3, 66–74.
- 661 Schmidt, C., and Seward, T.M. (2017) Raman spectroscopic quantification of sulfur species in  
662 aqueous fluids: Ratios of relative molar scattering factors of Raman bands of H<sub>2</sub>S, HS<sup>-</sup>,  
663 SO<sub>2</sub>, HSO<sub>4</sub><sup>-</sup>, SO<sub>4</sub><sup>2-</sup>, S<sub>2</sub>O<sub>3</sub><sup>2-</sup>, S<sub>3</sub><sup>-</sup> and H<sub>2</sub>O at ambient conditions and information on changes  
664 wit. *Chemical Geology*, 467, 64–75.
- 665 Schmidt, C., and Watenphul, A. (2010) Ammonium in aqueous fluids to 600 °C, 1.3 GPa: A  
666 spectroscopic study on the effects on fluid properties, silica solubility, and K-feldspar to  
667 muscovite reactions. *Geochimica et Cosmochimica Acta*, 74, 6852–6866.
- 668 Schmidt, C., and Ziemann, M.A. (2000) In-situ Raman spectroscopy of quartz: A pressure sensor  
669 for hydrothermal diamond-anvil cell experiments at elevated temperatures. *American*  
670 *Mineralogist*, 85, 1725–1734.
- 671 Schmidt, C., Steele-MacInnis, M., Watenphul, A., and Wilke, M. (2013) Calibration of zircon as  
672 a Raman spectroscopic pressure sensor to high temperatures and application to water-  
673 silicate melt systems. *American Mineralogist*, 98, 643–650.
- 674 Schroetter, H., and Kloeckner, H.W. (1979) Raman scattering cross sections in Gases and  
675 Liquids. In *Raman Spectroscopy of Gases and Liquids* pp. 123–166.
- 676 Self, S. (2005) Effects of volcanic eruptions on the atmosphere and climate. In J. Marti and  
677 G.G.J. Ernst, Eds., *Volcanoes and the Environment* pp. 152–174. Cambridge University  
678 Press, UK.

- 679 Self, S., and Blake, S. (2008) Consequences of explosive supereruptions. *Elements*, 4, 41–46.
- 680 Soper, A.K. (2000) The radial distribution functions of water and ice from 220 to 673 K and at  
681 pressures up to 400 MPa. *Chemical Physics*, 258, 121–137.
- 682 Symonds, R.B., Rose, W.I., Bluth, G.J.S., and T.M., G. (1994) Volcanic-gas studies; methods,  
683 results, and applications. *Reviews in Mineralogy*, 30, 1–66.
- 684 Wagner, W., and Pruß, A. (2002) The IAPWS formulation 1995 for the thermodynamic  
685 properties of ordinary water substance for general and scientific use. *Journal of Physical and*  
686 *Chemical Reference Data*, 31, 387–535.
- 687 Walrafen, G.E. (1964) Raman Spectral Studies of Oleums. *The Journal of Chemical Physics*, 40,  
688 3249.
- 689 Zielińska, M., Yavorska, M., Porêba, M., and Sieniawski, J. (2010) Thermal properties of cast  
690 nickel based superalloys. *Archives of Materials Science and Engineering*, 44, 35–38.
- 691



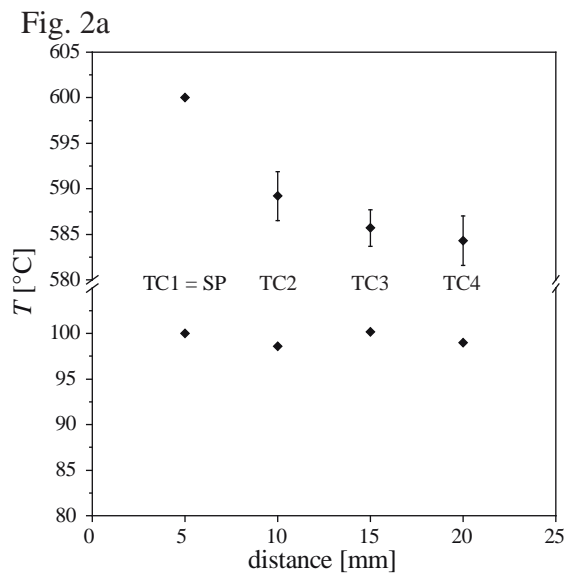


Fig. 2b

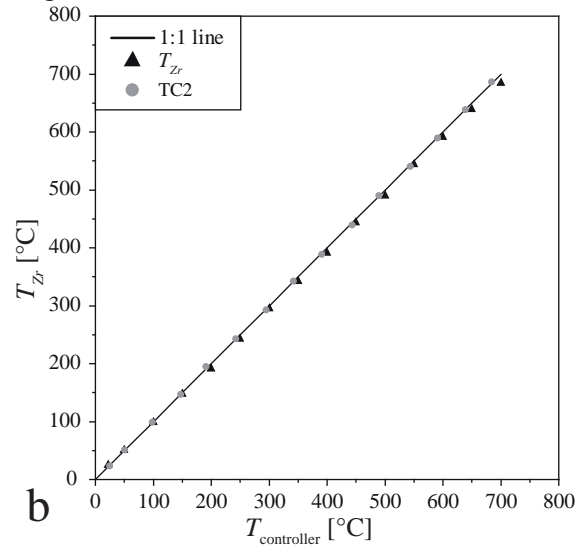


Fig. 3

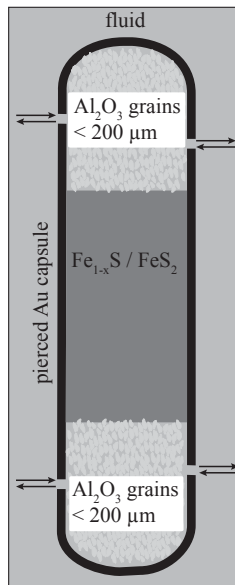


Fig. 4a

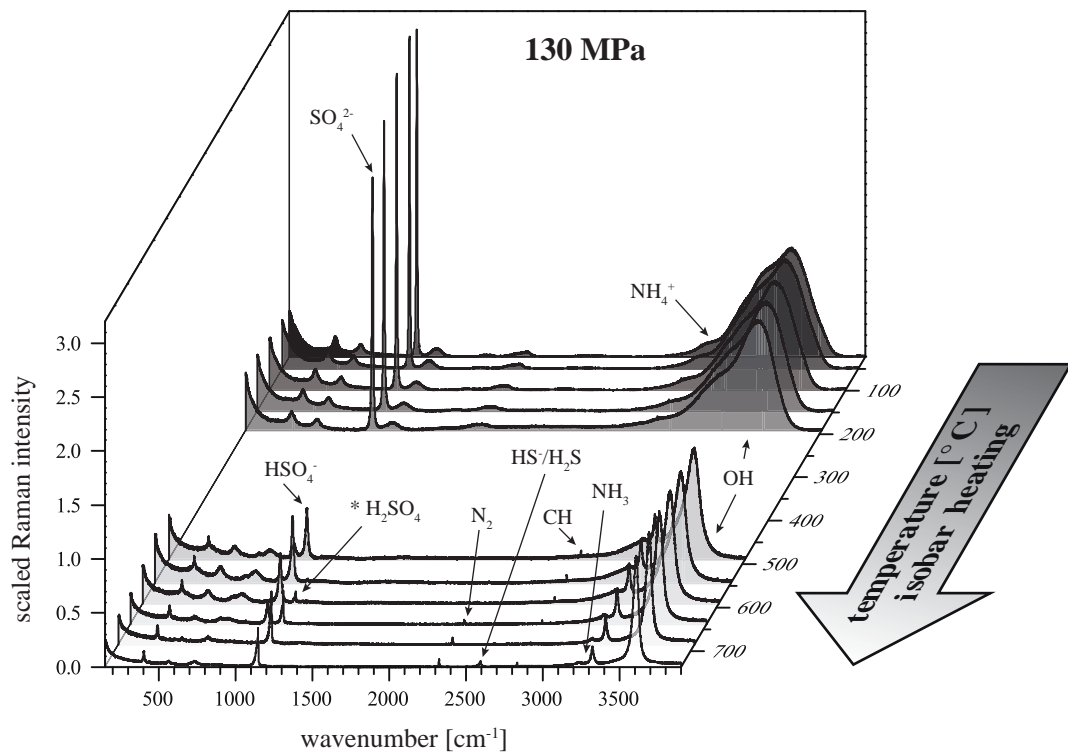


Fig. 4b

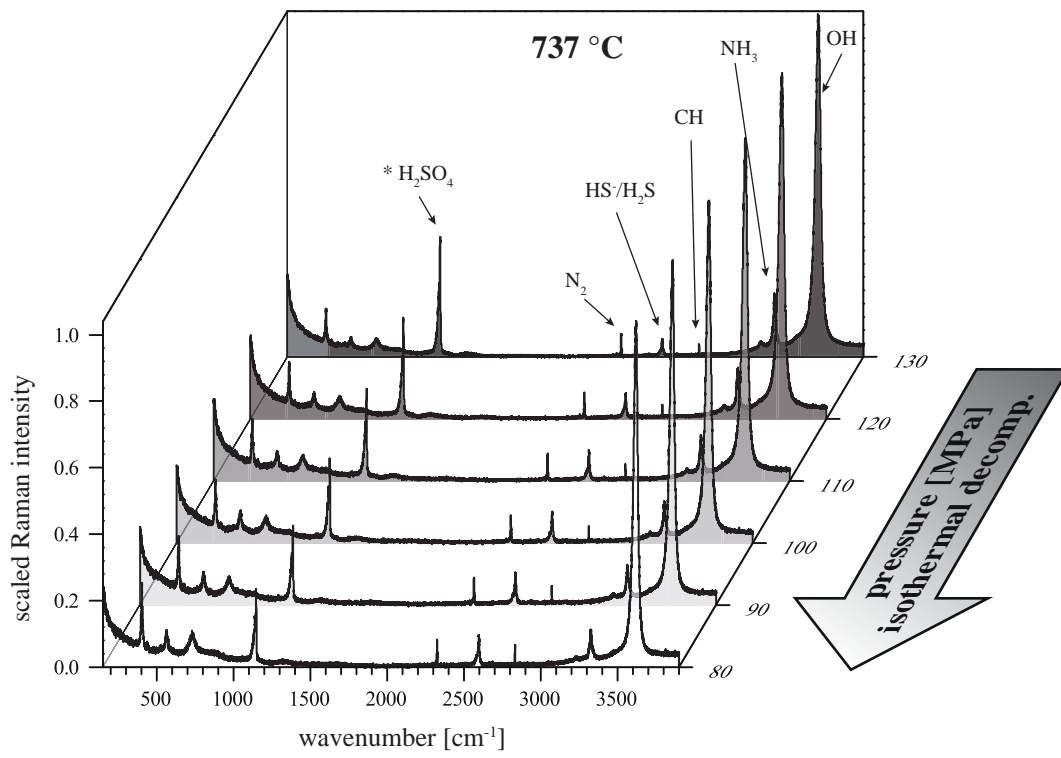


Fig. 4c

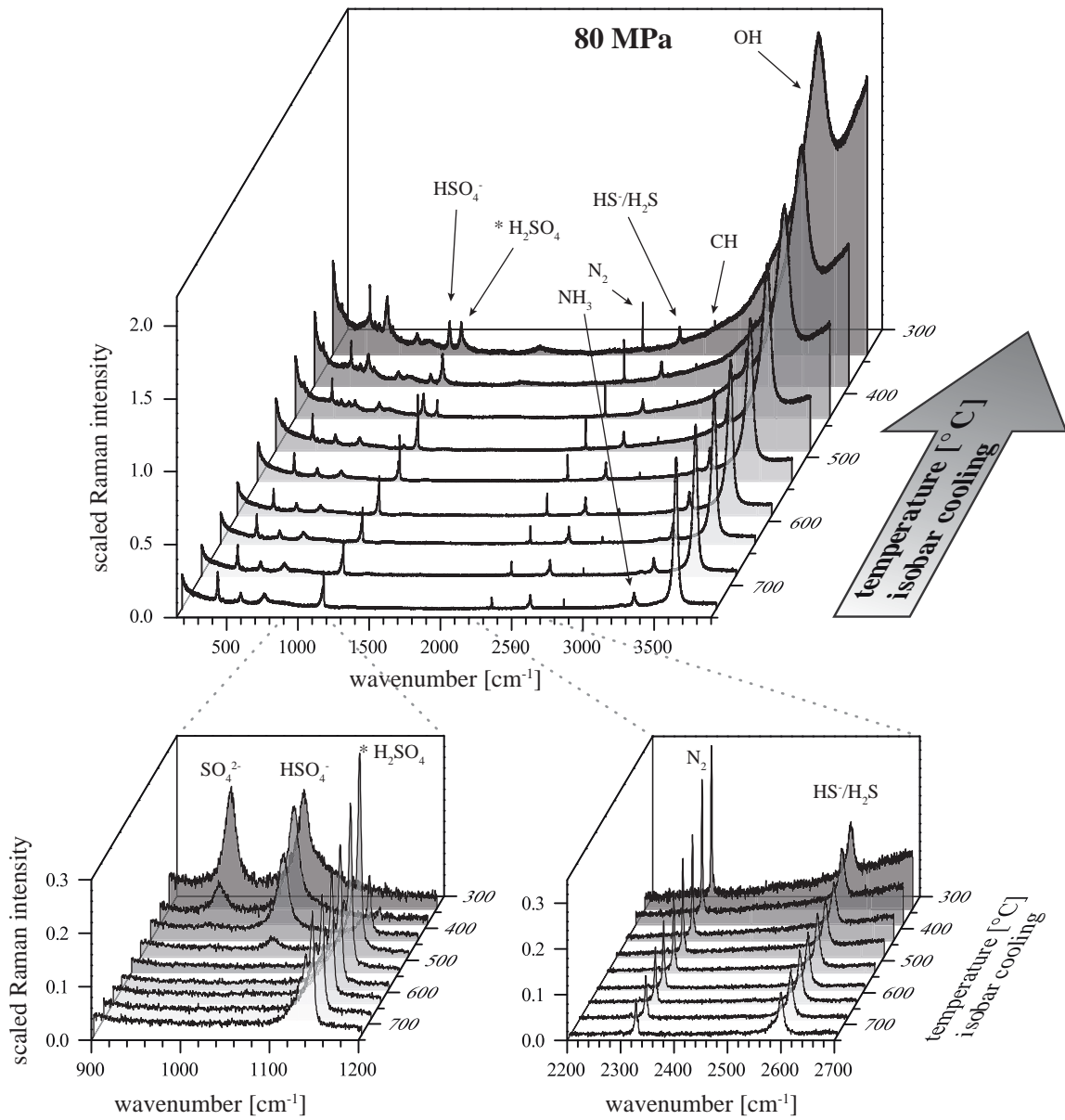


Fig. 5a

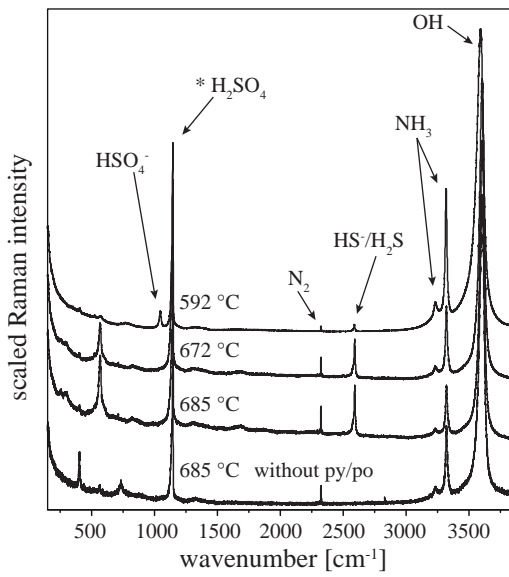


Fig. 5b

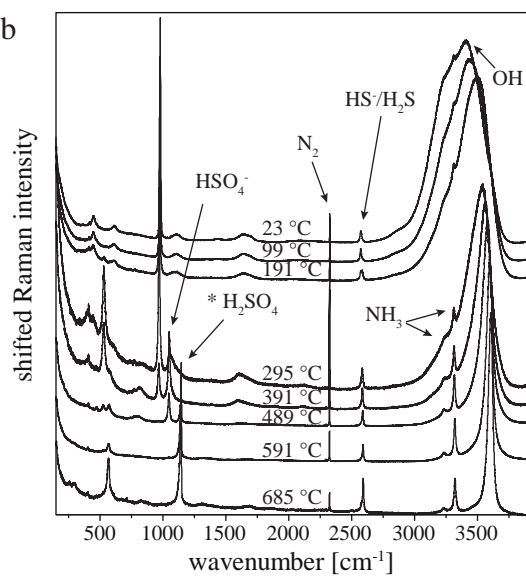


Fig. 6 a-h

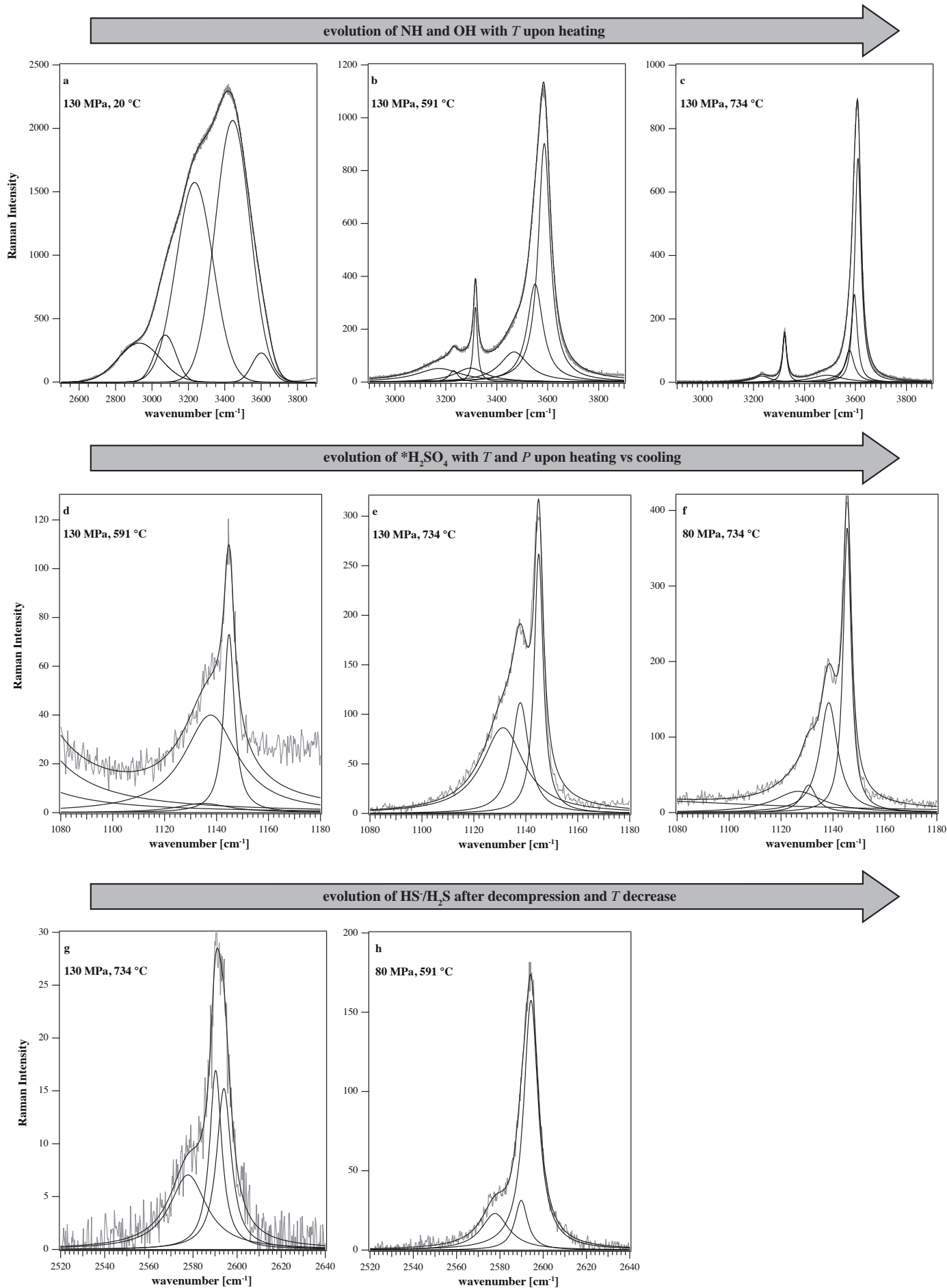


Fig. 7a  
130 MPa

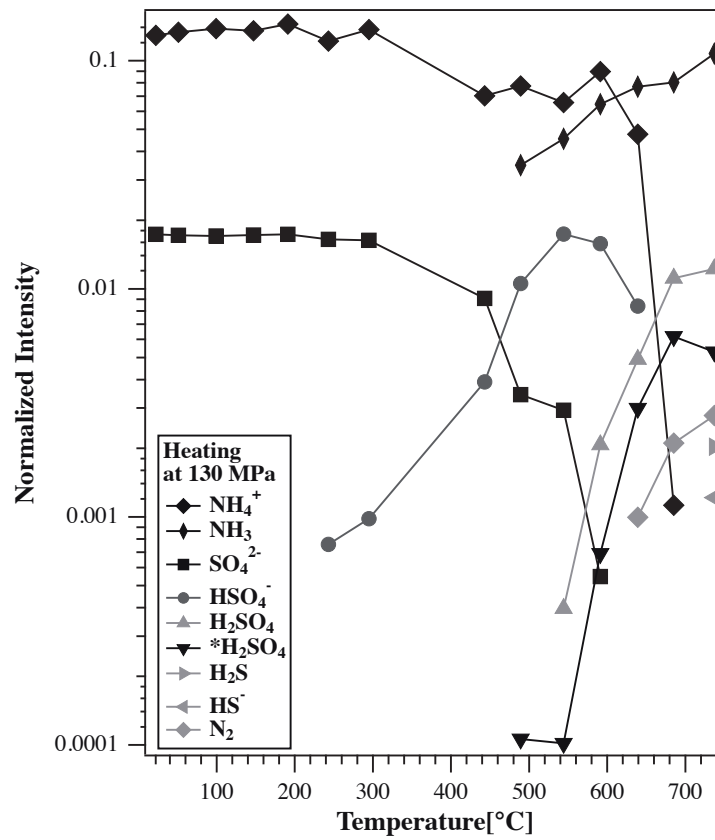


Fig. 7b  
734 °C

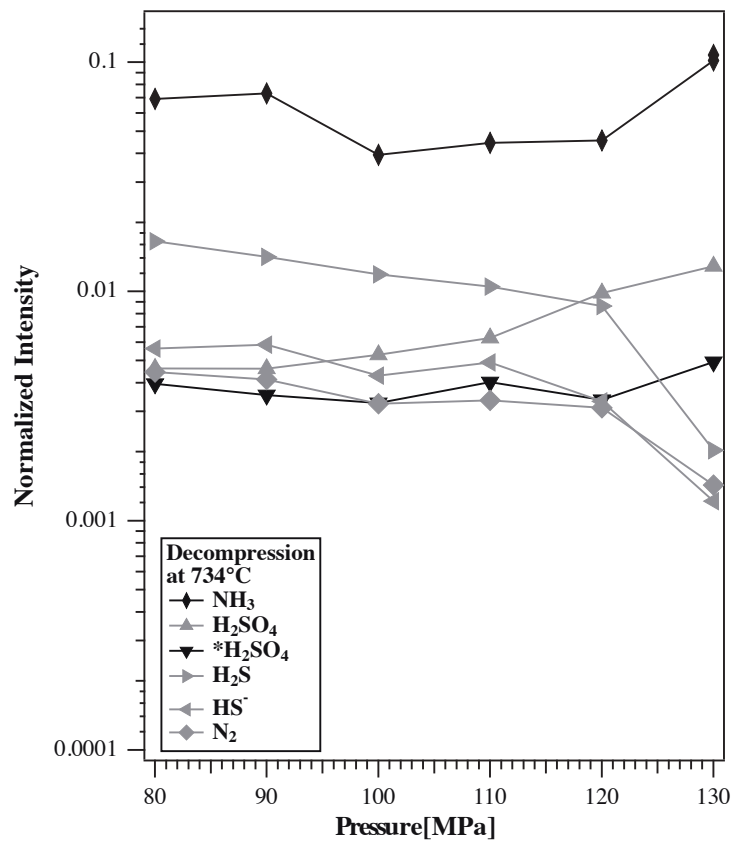


Fig. 7c  
80 MPa

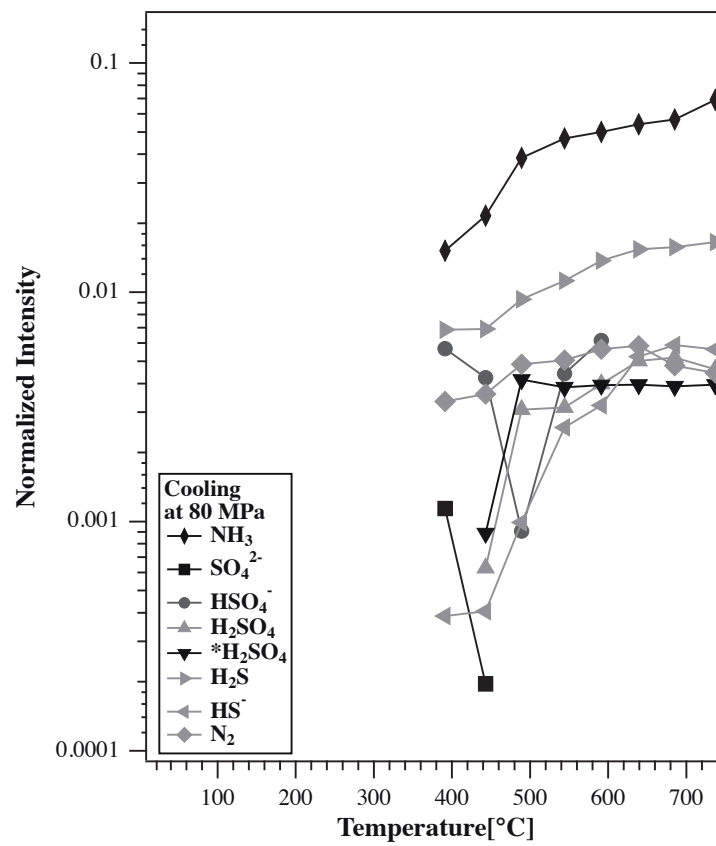


Fig. 8a  
pyrite, pyrrhotite  
130 MPa

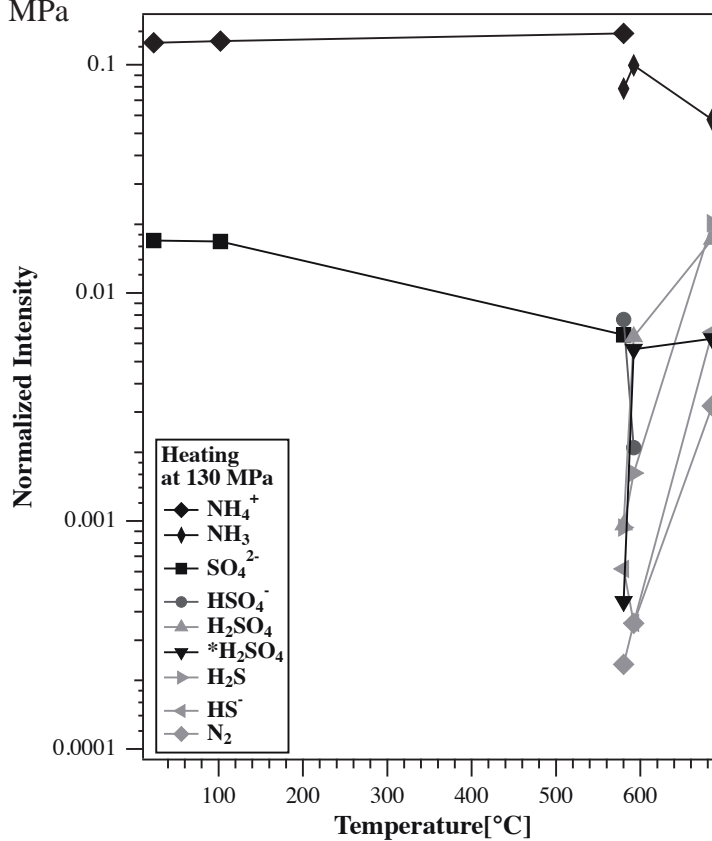
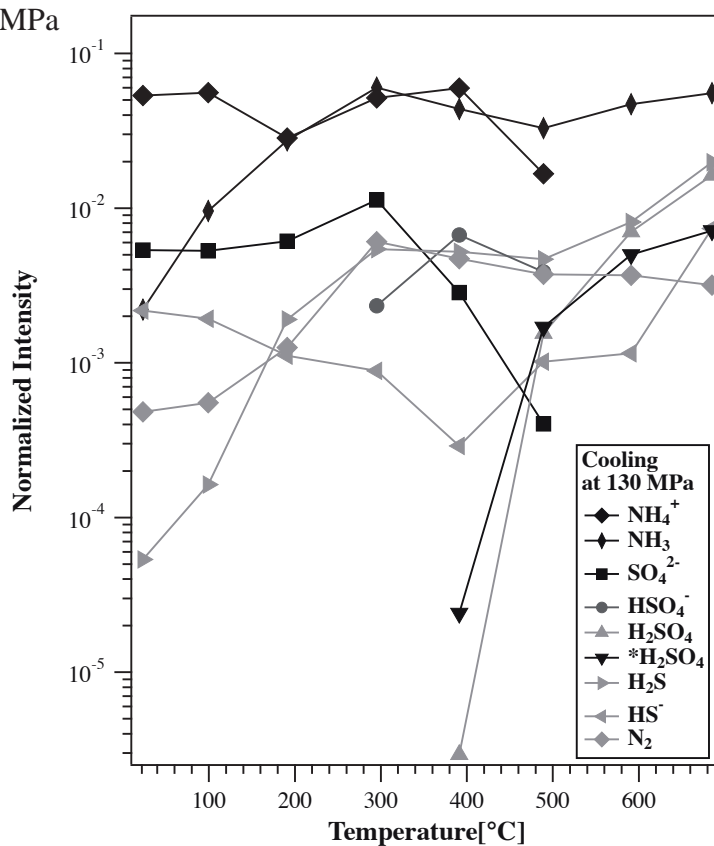


Fig 8b  
pyrite, pyrrhotite  
130 MPa



**Table 1.** Raman frequencies above 900 cm<sup>-1</sup> and species assignments at three temperatures

| Position<br>(cm <sup>-1</sup> ) | Species                       | Ref. | Position<br>(cm <sup>-1</sup> ) | Species   | Ref.  | Position<br>(cm <sup>-1</sup> ) | Species   | Ref.  |
|---------------------------------|-------------------------------|------|---------------------------------|---|-------|---------------------------------|---|-------|
| 19°C                            |                               |      | 544°C                           |   |       | 737°C                           |   |       |
| 980                             | SO <sub>4</sub> <sup>2-</sup> | 1,2  | 964                             | SO <sub>4</sub> <sup>2-</sup>                     | 1,2   | 1047                            | HSO <sub>4</sub> <sup>-</sup>                     | 1     |
| 2930                            | NH <sub>4</sub> <sup>+</sup>  | 8    | 1039                            | HSO <sub>4</sub> <sup>-</sup>                     | 1     | 1131                            | H <sub>2</sub> SO <sub>4</sub>                    | 3     |
| 3073                            | NH <sub>4</sub> <sup>+</sup>  | 8,9  | 1047                            | HSO <sub>4</sub> <sup>-</sup>                     | 1     | 1138                            | H <sub>2</sub> SO <sub>4</sub>                    | 3     |
| 3234                            | H <sub>2</sub> O              | 8,9  | 1138                            | H <sub>2</sub> SO <sub>4</sub>                    | 3     | 1145                            | SO <sub>2</sub> , *H <sub>2</sub> SO <sub>4</sub> | 3, 11 |
| 3443                            | H <sub>2</sub> O              | 8,9  | 1145                            | SO <sub>2</sub> , *H <sub>2</sub> SO <sub>4</sub> | 3, 11 | 2323                            | N <sub>2</sub>                                    | 7     |
| 3601                            | H <sub>2</sub> O              | 8,9  | 3165                            | NH <sub>4</sub> <sup>+</sup>                      | 10    | 2578                            | HS <sup>-</sup>                                   | 4,5,6 |
|                                 |                               |      | 3231                            | NH <sub>3</sub>                                   | 10    | 2594                            | H <sub>2</sub> S                                  | 4,5,6 |
|                                 |                               |      | 3314                            | NH <sub>3</sub>                                   | 8,9   | 3232                            | NH <sub>3</sub>                                   | 10    |
|                                 |                               |      | 3270                            | H <sub>2</sub> O                                  | 8,9   | 3322                            | NH <sub>3</sub>                                   | 10    |
|                                 |                               |      | 3436                            | H <sub>2</sub> O                                  | 8,9   | 3488                            | H <sub>2</sub> O                                  | 8,9   |
|                                 |                               |      | 3576                            | H <sub>2</sub> O                                  | 8,9   | 3576                            | H <sub>2</sub> O                                  | 8,9   |
|                                 |                               |      |                                 |   |       | 3596                            | H <sub>2</sub> O                                  | 8,9   |
|                                 |                               |      |                                 |   |       | 3610                            | H <sub>2</sub> O                                  | 8,9   |

Notes. Positions represent the band maxima from fitting as shown in Figures 7, except for 1

different temperatures  $\alpha$

$\alpha_2$  where peak positions we